JVI Accepted Manuscript Posted Online 8 September 2020
J. Virol. doi:10.1128/JVI.01683-20

Disruption of Adaptive Immunity Enhances Disease in SARS-CoV-2 Infected Syrian Hamsters

Running Title: Severe disease hamster model of SARS-CoV-2

Authors: Rebecca L. Brocato[a], Lucia M. Principe[a], Robert K. Kim[b], Xiankun Zeng[b], Janice A. Williams[b], Yanan Liu[c], Rong Li[c], Jeffrey M. Smith[a], Joseph W. Golden[a], Dave Gangemi[d,e], Sawsan Youssef[d,e], Zhongde Wang[c], Jacob Glanville[d,e], and Jay W. Hooper[a#]

Affiliations:

[a]Virology Division, United States Army Research Institute of Infectious Diseases, Frederick, MD

[b]Pathology Division, United States Army Research Institute of Infectious Diseases, Frederick, MD

[c]Department of Animal, Dairy and Veterinary Sciences, Utah State University, Logan, UT

[d] Distributed Bio, Inc. South San Francisco, CA

[e] Centivax, Inc. South San Francisco, CA

#Correspondence to: jay.w.hooper.civ@mail.mil

Word Count:

Abstract: 149 (abstract), 125 (importance)

Main Text: 4,370

Abstract

Animal models recapitulating human COVID-19 disease, especially with severe disease, are urgently needed to understand pathogenesis and evaluate candidate vaccines and therapeutics. Here, we develop novel severe disease animal models for COVID-19 involving disruption of adaptive immunity in Syrian hamsters. Cyclophosphamide (CyP) immunosuppressed or *RAG2* knockout (KO) hamsters were exposed to SARS-CoV-2 by the respiratory route. Both the CyP-treated and *RAG2* KO hamsters developed clinical signs of disease that were more severe than in immunocompetent hamsters, notably weight loss, viral loads, and fatality (*RAG2* KO only). Disease was prolonged in transiently immunosuppressed hamsters and uniformly lethal in *RAG2* KO hamsters. We evaluated the protective efficacy of a neutralizing monoclonal antibody and found that pretreatment, even in immunosuppressed animals, limited infection. Our results suggest that functional B and/or T cells are not only important for the clearance of SARS-CoV-2, but also play an early role in protection from acute disease.

Importance

Syrian hamsters are in use as a model of disease caused by SARS-CoV-2. Pathology is pronounced in the upper and lower respiratory tract and disease signs and endpoints include weight loss, viral RNA and/or infectious virus in swabs and organs (e.g. lungs). However, a high dose of virus is needed to produce disease and the disease resolves rapidly. Here, we demonstrate that immunosuppressed hamsters are susceptible to low doses of virus and develop more severe and prolonged disease. We demonstrate the efficacy of a novel neutralizing monoclonal antibody using the cyclophosphamide transient suppression model. Furthermore, we demonstrate that RAG2 knockout hamsters develop severe/fatal disease when exposed to

SARS-CoV-2. These immunosuppressed hamster models provide researchers new tools for evaluating therapies and vaccines, and understanding COVID-19 pathogenesis.

Introduction

The ongoing pandemic has led to the search for animal models faithfully recapitulating salient features of human coronavirus disease (COVID-19) for pathogenesis studies and evaluation of vaccines and therapeutics (1). Early reports indicated that Syrian hamsters, whose ACE2 is highly homologous to its human ortholog, were highly susceptible to SARS-CoV-2 infection but did not develop severe disease (2, 3). In 2008, administration of cyclophosphamide (CyP), an alkylating agent that suppresses B and T cell function, was used to develop a severe disease model for SARS-CoV in Syrian hamsters (4). We reasoned that a similar approach might allow the development of a severe disease model for SARS-CoV-2. Moreover, clinical findings of lymphopenia associated with COVID-19 (5) and its prominence in severe cases (6, 7) suggested an immunosuppressed animal model of COVID-19 might more accurately model some aspects of severe human disease. Here, we used CyP-treated and *RAG2* KO hamsters to investigate how transient disruption, or ablation, of the adaptive immune response affects SARS-CoV-2 infection. In addition, we used the immunocompetent and immunosuppressed hamster models to evaluate whether pre-exposure to virus through previous infection, or neutralizing antibodies, were sufficient to limit or prevent disease.

Results

Transient immunosuppression using CyP increased duration and severity of disease in SARS-CoV-2 infected hamsters.

In our first experiment manipulating the adaptive immune response, we immunosuppressed hamsters using CyP (CyP-Tx) beginning -3 dpi. Suppression of lymphocytes was confirmed by hematology analysis just prior to challenge (**Fig. 1A**). On Day 0, groups of 10 hamsters were

exposed to 100, 1,000, or 10,000 PFU of SARS-CoV-2 by the intranasal route. Disease progression was monitored by weight loss (**Fig. 1B**) and detection of viral RNA in pharyngeal swab using RT-PCR (**Fig. 1C**). Weight loss was remarkably similar between all SARS-CoV-2 exposed groups regardless of dose, with drastic weight loss beginning 6 dpi. Weight loss remained significant relative to starting weight through 35 dpi. In contrast, mock (PBS) challenged hamsters treated with CyP steadily gained weight with a few exceptions. Specifically, one cage of four mock challenged hamsters showed evidence of weight loss 9-12 dpi. These same animals were the only mock challenged hamsters that were positive in the SARS-CoV-2 pharyngeal swab RT-PCR analysis starting 9 dpi (**Fig 1C**).

All of the SARS-CoV-2 challenged hamsters had detectable viral RNA in pharyngeal swabs at the first time point assayed, 3 dpi, and remained consistent (10^3-10^5 molecules of N2 per 100ng RNA) through the duration of CyP treatment (**Fig 1C**). After the last CyP treatment on 21 dpi, most of the hamsters continued to lose weight and several hamsters began to exhibit signs of a wasting disease, *i.e.* cachexia and extreme weight loss, requiring euthanasia (**Fig. 1B,D)**. Then, approximately 7 days after cessation of CyP the remaining hamsters started gaining weight and viral RNA levels in pharyngeal swabs dropped below 10^3 molecules of N per 100 ng RNA (**Fig. 1C**). Viral RNA and infectious virus was detected in lung tissue from a subset of hamsters collected 13 dpi, the day of euthanasia of moribund animals (14-34 dpi), or euthanasia 35 dpi (end of study, **Fig. 1E,F**). There was a statistically significant reduction in lung viral burden comparing 35 dpi to 13 dpi lung homogenates. Serum collected from surviving hamsters 35 dpi was assayed for neutralizing antibodies (**Fig. 1G**). Six of the ten infected hamsters that survived in the CyP immunosuppression experiment never developed detectable levels of neutralizing antibodies. Interestingly, the four hamsters that did develop neutralizing antibodies after CyP

treatment cessation rebounded more rapidly as measured by weight gain (**data not shown**). Together these data indicate that CyP treatment allowed a persistent infection that was reversed, in most animals, when CyP treatment was stopped and the adaptive immune response allowed to recover.

RAG2 KO hamsters infected with SARS-CoV-2 results in a lethal model

RAG2 KO hamsters deficient in recombination activation gene 2 do not produce functional T or B cells (8). Whereas CyP treatment allowed transient and partial immunosuppression, the *RAG2* KO hamsters allowed us to evaluate the outcome of SARS-CoV-2 infection in the absence of functional lymphocytes. *RAG2* KO hamsters were exposed to 10,000 PFU SARS-CoV-2 by the intranasal route. The *RAG2* KO hamsters showed significant weight loss starting 3 dpi (**Fig. 2A**) and the infection was uniformly lethal with a median day-to-death of 6 days (p=0.0025, Log-rank test, **Fig. 2B**). Viral RNA detected from pharyngeal swabs trended to be higher than the CyP-treated hamsters, but not statistically significant (**Fig. 2C**). The 10,000 PFU and PBS mock groups from the CyP experiment shown in **Fig. 1** were included in **Fig. 2A-C** for comparison. Organs from the *RAG2* KO animals that succumbed or met euthanasia criteria were homogenized and evaluated for viral RNA by RT-PCR. Viral RNA was present at the highest levels in the lung and trachea. Lower levels of viral RNA were also detected in extrapulmonary organs including the heart, liver, spleen, intestine, brain and kidney (**Fig. 2D**).

Increased pathology of SARS-CoV-2-infected *RAG2* KO hamsters includes hemorrhage and severe edema

A subset of the SARS-CoV-2-infected hamsters from the CyP experiment shown in **Fig. 1** were euthanized 13 dpi. Lungs were formalin-fixed, paraffin embedded, and evaluated by histopathology and *in situ* hybridization (ISH) (**Fig. 3**). Lung tissue from necropsied animals

120 demonstrated focally extensive areas consolidation of pulmonary parenchyma admixed with
121 dense aggregates of inflammatory cells (**Fig. 3A**). The bronchial lumina are multi-focally lined
122 by hyperplastic respiratory epithelium (**Fig. 3B**) and SARS-CoV-2 genomic RNA was frequently
123 detected in alveolar pneumocytes, alveolar infiltrates, and bronchiolar epithelial cells by ISH
124 (**Fig. 3C**). At 14 dpi, immunocompetent hamsters infected with SARS-CoV-2 exhibited only
125 mild congestion and inflammatory infiltration indicating recovery from viral challenge (2)
126 supporting the hypothesis that CyP administration to disrupt adaptive immunity exacerbates and
127 prolongs disease in hamsters.

128 Lung tissue collected at the time of death of SARS-CoV-2-infected *RAG2* KO hamsters contain
129 areas of hemorrhage and inflammation expanding the interstitium and connective tissue
130 surrounding bronchi and arteries (**Fig. 3D**). As seen in the CyP-treated hamsters, the bronchial
131 lumina of *RAG2* KO hamsters is lined with multiple layers of infected epithelial and club cells,
132 containing infiltrates of lymphocytes (presumably nonfunctional), heterophils and macrophages
133 (**Fig. 3E,G,H**). There is hemorrhage within alveolar lumen and consolidation with septal
134 congestion. Also as observed in CyP-treated hamsters, SARS-CoV-2 genomic RNA and viral
135 antigen were frequently detected in alveolar pneumocytes (**Fig. 3I**), alveolar infiltrates, and
136 bronchiolar epithelial cells (**Fig. 3F**). Together these data indicate that the absence of functional
137 B and T cells in *RAG2* KO hamsters allows increased pathology and lethality from SARS-CoV-2
138 infection.

139 Electron microscopy studies were performed on lung sections of SARS-CoV-2 infected, CyP-
140 treated hamsters with varying lung viral loads (**Fig. 1**). The lungs lack a typical morphology
141 wherein distinct alveolar, inter-alveolar septum with capillaries, Type I and Type II pneumocytes
142 are clearly evident. The animal with the least viral load (10^6 molecules of N2 per 100ng RNA,

Fig. 3J) show some remnants of normal architecture while the animal with the highest viral load (10^8 molecules of N2 per 100ng RNA, **Fig. 3L**) lack the prominent alveolar space and were congested with immune cells. The lamellar bodies in the Type II pneumocytes are still identifiable in hamsters with high viral loads.

SARS-CoV-2 is reported to range in diameter from 50-160nm (with surface spikes measuring approximately 20nm) (9-13). The low and high viral load samples show compartmentalized vacuoles with round virus-like structure and vesicles with irregular shaped structures, resembling multi-vesicular bodies (**Fig. 3J-L**). The more electron dense vesicles are suggestive of mature virus particles whereas, the less electron dense particles are likely immature virions. In addition to cytoplasmic vacuoles, these tissue show swollen rough endoplasmic reticulum (rER, **Fig. 3L**). Swollen rER appears as a result of cellular stress and/or increased viral protein synthesis. Immuno-gold labeling is necessary to confirm the presence of virus particles.

Tracheas from the same SARS-CoV-2 infected, CyP-treated hamsters with varying lung viral loads were analyzed by electron microscopy. These tracheas also exhibit disruption of the epithelial layer. Trachea from the animal with the lowest lung viral load (10^6 molecules of N2 per 100ng RNA) showed mostly intact ciliated cells on the surface (**Fig. 4A**). These cells show several cytoplasmic vacuoles with potential immature virus particles (**Fig. 4D,E**). As lung viral load increases, the presence of ciliated cells and epithelial cells lining the tracheal lumen decrease (**Fig. 4B-C**, respectively). Very few ciliated cells were seen in the animals with the heaviest viral load (10^8 molecules of N2 per 100ng RNA) and there is an absence of cytoplasmic content marked by the lack of electron dense cytoplasmic vesicles (**Fig. 4F**).

Protective efficacy of prior SARS-CoV-2 infection

Nine previously infected immunocompetent hamsters from two separate experiments were retained for a re-challenge with SARS-CoV-2. Our goal was to determine if prior infection elicited protective immunity. To ensure that these hamsters had cleared infectious virus after the initial challenge, hamsters were treated with 3 doses of CyP and weights monitored for 14 days (**Fig. 5A**). If the animals were persistently infected, we predicted that hamsters would experience onset of disease as measured by rapid weight loss and positive pharyngeal swab RT-PCR following CyP administration. No significant weight loss was detected and swabs were negative for viral RNA (**Fig. 5A**). All nine animals were positive for neutralizing antibodies prior to the re-challenge (**Fig. 5B**). The nine previously exposed hamsters and seven naïve hamsters were challenged with 100,000 PFU SARS-CoV-2. Weights were monitored daily and pharyngeal swabs were collected every other day for viral RNA RT-PCR. Control animals lost weight as predicted whereas the previously exposed animals were protected from significant weight loss. Pharyngeal swab RT-PCR indicated a statistically significant reduction in viral RNA detected in re-challenged animals compared to naïve animals (**Fig. 5C**). In addition, viral load in lung homogenates from animals euthanized at the end of the study indicated a statistically significant ($p=0.0164$, unpaired t test) reduction in viral RNA level in the re-challenged animals **Fig. 5D**). There was no infectious virus in the lungs on of the re-challenged hamster 7 days after exposure. However, only two of the naïve hamsters had infectious virus after challenge (**Fig. 5E**). The likely reason for the disappearance of infectious virus in the lungs of the naïve group is that those animals had already mounted an immune response and infectious virus was cleared by the time the lung samples were collected. Altogether, these data indicate immunocompetent hamsters that had recovered from prior exposure to the SARS-CoV-2 were not persistently infected, but instead were protected (i.e., protective immunity).

Protective efficacy of anti-SARS-CoV-2 mAb

A human monoclonal antibody (mAb) targeting the spike protein of SARS-CoV-2 was evaluated in a passive transfer experiment using immunosuppressed hamster. Thirty mg/kg of Centi-F1 mAb (IC50= 391 ng/mL, PRNT80=1280), a control IgG (normal) mAb, or PBS were administered -1 dpi. On Day 0 the immunosuppressed animals were challenged with 1,000 PFU SARS-CoV-2. Neutralizing antibody levels in sera at the time of challenge were measured by PRNT80 (**Fig. 6A**). Detectable levels ranging from 80 to ≥640 were found in the Centi-F1 mAb group. Disease progression was monitored by weight change (**Fig. 6B**) and pharyngeal swab RT-PCR (**Fig. 6C**). Hamsters administered the normal mAb or PBS exhibited significant weight loss starting 5 dpi and ultimately had group weights drop to 86% and 91%, respectively. Hamsters Treated with Centi-F1 mAb maintained over 100% of their Day 0 weight to the conclusion of the experiment (13 dpi). Virus RNA was detected in pharyngeal swabs in all groups but trending lower in Centi-F1 mAb-treated animals on Day 11 ($p=0.1038$, unpaired t test). Similarly, lung tissue collected 13 dpi (end of study) indicate comparable levels of viral RNA detected (**Fig. 6D**), but significantly reduced infectious virus in Centi-F1 mAb-treated animals ($p=0.0002$, unpaired t test, **Fig. 6E)**. These findings demonstrate that a SARS-CoV-2 mAb can limit infection in immunosuppressed animals.

Discussion

It has been postulated that both innate immune hyperactivity and adaptive immune dysfunction result in increased SARS-CoV-2 dissemination and drives severe disease (14). In order to develop a small animal model of severe disease, evaluate the role of adaptive immunity, and replicate the COVID-19 lymphopenia observed in human disease, we treated hamsters with CyP. In this immunosuppressed model, we observe more drastic weight loss, high levels of virus in the

lung, and viral persistence that did not begin to resolve until CyP treatment was stopped (**Fig. 1**). Histopathologic findings in the lungs of CyP-treated hamsters also demonstrate the prolonged pathology and ongoing repair through hyperplastic changes of the bronchial epithelium and type II pneumocytes that were not observed in the sampled *RAG2* KO hamsters. These data demonstrate the critical role B and T cells play in resolution of disease, and describe an animal model for severe COVID-19 disease that can be used for rigorous testing of medical countermeasures.

The recent development of immune function KO hamsters combined with Syrian hamster susceptibility to SARS-CoV-2 infection allows investigation of the role of a specific immune functions in COVID-19 pathogenesis and protection. Thus far, *STAT2* KO hamsters have been used to demonstrate that type I interferon plays a role in restricting viral dissemination and promoting lung pathology in SARS-CoV-2 infected animals (15). Herein we found, unexpectedly, that SARS-CoV-2 challenge resulted in a uniform lethality in the *RAG2* KO hamsters. It is interesting that onset of disease, as measured by weight loss, was more rapid (by 3 days) in the *RAG2* KO animals than immunocompetent, or even transiently immunosuppressed, hamsters receiving the same challenge dose. This indicates that the absence of functional B cells and/or T cells exacerbates pathogenesis at a very early stage (within a day or two) after exposure to virus. The importance of T cells in viral clearance has been noted for other coronaviruses, SARS-CoV (16) and MERS (17). In fact, depletion of CD3+ T cells correlates with severity and adverse outcomes (18).

There have been anecdotal accounts suggesting that immunity generated from an initial SARS-CoV-2 infection in humans may not be protective against a subsequent infection. Recent studies using nonhuman primates indicated prior infection results in protective immunity (19). Here, we

show that the immune response from an initial SARS-CoV-2 infection, including a robust neutralizing antibody response, is protective against re-challenge. We detected reduced levels of viral RNA in pharyngeal swabs and lungs, however, despite circulating neutralizing antibody available at the time of challenge, virus RNA was still detected seven days after re-challenge. Viral RNA in pharyngeal swabs on Day 5 following re-challenge and in lung tissue on Day 7 could indicate that asymptomatic reinfection is possible. Prolonged viral shedding has been observed in human COVID-19 cases, with detectable neutralizing antibody titers (20). Alternatively, the RNA detected in the swabs could be input virus that is slowly being cleared from the respiratory system.

Currently, convalescent plasma is an option to treat severe cases of COVID-19 (21). Another antibody-based options include manufactured polyclonal or mAbs that represent avenues to prevent or treat SARS-CoV-2 infections as a standardized product. Several groups have reported *in vitro* characterization of anti-SARS-CoV-2 neutralizing mAbs and a number of antibodies have been shown to protect in small animal models, including Syrian hamsters (22, 23). Here, pre-treatment with mAb Centi-F1 resulted in weight maintenance through the experiment, trending lower levels of viral RNA detected in pharyngeal swabs and lung tissues, and most importantly, reduced levels of infectious virus detected in the lung. The lack of statistical significance in pharyngeal swabs and lung homogenates could possibly be obviated using a subgenomic RNA assay; however, passive transfer of IgG failing to adequately protect the upper airway (24) may also play a role.

Our results expand on the earlier findings that the Syrian hamster model is a suitable small animal model of COVID-19 (2). Transient and reversible immunosuppression using CyP can be used to increase the severity and duration of the disease state. Advantages of the CyP model are

that the wild type hamsters are readily available, and would produce a normal immune response to vaccination. One disadvantage is that disruption of lymphocytes could confound the evaluation of therapeutics that target components of the immune response, or vaccines that require rapid mobilization of the adaptive response. For evaluation of those types of medical countermeasures, the wild type hamster would be preferred. This is the first report that SARS-CoV-2 is lethal in *RAG2* KO hamsters. For practical purposes, uniformly lethal models allow fewer numbers of animals to detect significant levels of protection facilitating rapid screening of candidate therapeutics. *RAG2* KO hamsters would not be suitable for the use in active vaccine studies but could be used for antibody passive transfer studies. For example, passive transfer of immune serum from nonhuman primate or human vaccine studies could be an approach to investigate mechanisms of protection. Overall, our hamster SARS-CoV-2 models with severe diseases clinically relevant to those of COVID-19 patients provide a platform for evaluating candidate medical countermeasures to combat the pandemic.

Materials and Methods

Ethics. Animal research was conducted under an IACUC approved protocol at USAMRIID (USDA Registration Number 51-F-00211728 & OLAW Assurance Number A3473-01) in compliance with the Animal Welfare Act and other federal statutes and regulations relating to animals and experiments involving animals. The facility where this research was conducted is fully accredited by the Association for Assessment and Accreditation of Laboratory Animal Care, International and adheres to principles stated in the Guide for the Care and Use of Laboratory Animals, National Research Council, 2011.

SARS-CoV-2 stock. An aliquot of the third passage of SARS-CoV-2 USA-WA-1/2020 was received from the CDC and propagated in ATCC Vero 76 cells (99% confluent) in EMEM

containing 1% GlutaMAX, 1% NEAA, and 10% heat-inactivated fetal bovine serum at an MOI of 0.01. Supernatant was collected from cultures exhibiting characteristic CPE and clarified by centrifugation (10,000 g x 10 minutes). Clarified virus was subjected to the following specifications: Identification by SARS-CoV-2 RT-PCR assay, Quantification by agarose-based plaque assay, free from contaminants by growth of chocolate agar plates, endotoxin testing using Endosafe® nexgen-PTS, and mycoplasma using MycoAlert test kit, and genomic sequencing. For experiments with a challenge dose of ≤10,000 PFU, virus p5 was used; for experiments with a challenge dose of 100,000 PFU, p6 was used. Genomic analysis indicates no changes between p3, p5, and p6 lots.

Animal Procedures. Wild type (females only, aged 6-8 weeks) or RAG2 KO (females and males, aged 11-12 weeks) hamsters (*Mesocricetus auratus*) were anesthetized by inhalation of vaporized isoflurane using an IMPAC6 veterinary anesthesia machine for the following procedures: intranasal challenge of virus, CyP intraperitoneal injections, pharyngeal swabs, and non-terminal blood collection. Intranasal instillation of SARS-CoV-2 was administered in a volume of 50µl for challenge doses of 100, 1,000 and 10,000 PFU, and 100µl for the challenge dose of 100,000 PFU. CyP treatment (Baxter, pharmaceutical grade) consisted of an initial loading dose of 140mg/kg, followed by maintenance doses of 100mg/kg on the days indicated by each experiment. Pharyngeal swabs in 0.5ml of complete media were used for virus detection to monitor infection and disease course in hamsters. Vena cava blood collection was limited to 7% of total blood volume per week. Terminal blood collection was performed by cardiac injection at the time of euthanasia. All work involving animals was performed in an animal biosafety level 3 (ABSL-3) laboratory.

Journal of Virology

Anti-SARS-CoV-2 mAb. F01 mAb was administered to hamsters at a dose of 30mg/kg by the subcutaneous route. F01 mAb was a kind gift from Distributed Bio, Inc.

Viral RNA assay. Following 3 freeze/thaws of frozen swabs in media, 250µl of media was removed and added to 750µl of Trizol LS. Approximately 200mg of organ tissue was homogenized in 1.0ml of Trizol using M tubes on the gentleMACS dissociator system on the RNA setting. RNA was extracted from Trizol LS or Trizol per manufacturer's protocol. A Nanodrop 8000 was used to determine RNA concentration, which was then raised to 100ng/µl in UltraPure distilled water. Samples were run in duplicate on a BioRad CFX thermal cycler using TaqPath 1-step RT-qPCR master mix according to the CDC's recommended protocol of 25°C for 2 minutes, 50°C for 15 minutes, 95°C for 2 minutes, followed by 45 cycles of , 95°C for 3 seconds and 55°C for 30 seconds. The forward and reverse primer and probe sequences are: 2019-nCoV_N2-F, 5'-TTA CAA ACA TTG GCC GCA AA-3', 2019-nCoV_N2-R, 5'-GCG CGA CAT TCC GAA GAA-3', and 2019-nCoV_N2-P, 5'-ACA ATT TCC CCC AGC GCT TCA G-3'. The limit of detection for this assay is 50 copies.

PRNT. An equal volume of complete media (EMEM containing 10% heat-inactivated FBS, 1% Pen/Strep, 0.1% Gentamycin, 0.2% Fungizone, cEMEM) containing SARS-CoV-2 was combined with 2-fold serial dilutions of cEMEM containing antibody and incubated at 37°C in a 5% CO_2 incubator for 1 hour (total volume 222µl). 180 µl per well of the combined virus/antibody mixture was then added to 6-well plates containing 3-day old, ATCC Vero 76 monolayers and allowed to adsorb for 1 hour in a 37°C, 5% CO_2 incubator. 3mL per well of agarose overlay (0.6% SeaKem ME agarose, EBME with HEPES, 10% heat-inactivated FBS, 100X NEAA, 1% Pen/Strep, 0.1% Gentamycin and 0.2% Fungizone) was then added and allowed to solidify at room temperature. The plates were placed in a 37°C, 5% CO_2 incubator for

2 days and then 2mL per well of agarose overlay containing 5% neutral red and 5% heat-inactivated FBS is added. After 1 additional day in a 37°C, 5% CO_2 incubator, plaques were visualized and counted on a light box. PRNT80 titers are the reciprocal of the highest dilution that results in an 80% reduction in the number of plaques relative to the number of plaques visualized in the cEMEM alone (no antibody) wells.

Plaque Assay. Approximately 200mg of lung tissue was homogenized in 1.0mL of cEMEM using a gentleMACS M tubes and a gentleMACS dissociator on the RNA setting. Tubes were centrifuged to pellet debris and supernatants collected. Ten-fold dilutions of the samples were adsorbed to Vero 76 monolayers (200µl of each dilution per well). Following a 1 hour adsorption in a 37°C, 5% CO_2 incubator, cells were overlaid and stained identically as described for PRNT. The limit of detection for this assay is 50 plaque forming units (PFU).

Hematology. Whole blood collected in EDTA tubes was analyzed on an HM5 hematology analyzer on the DOG2 setting.

Preparation of tissues for histology. Tissues were fixed in 10% neutral buffered formalin, trimmed, processed, embedded in paraffin, cut at 5 to 6µm, and stained with hematoxylin and eosin (H&E).

***In situ* hybridization.** To detect SARS-CoV-2 genomic RNA in FFPE tissues, *in situ* hybridization (ISH) was performed using the RNAscope 2.5 HD RED kit (Advanced Cell Diagnostics, Newark, CA, USA) as described previously (25). Briefly, forty ZZ ISH probes targeting SARS-CoV-2 genomic RNA fragment 21571-25392 (GenBank #LC528233.1) were designed and synthesized by Advanced Cell Diagnostics (#854841). Tissue sections were deparaffinized with xylene, underwent a series of ethanol washes and peroxidase blocking, and were then heated in kit-provided antigen retrieval buffer and digested by kit-provided proteinase.

Sections were exposed to ISH target probe pairs and incubated at 40°C in a hybridization oven for 2 h. After rinsing, ISH signal was amplified using kit-provided Pre-amplifier and Amplifier conjugated to alkaline phosphatase and incubated with a Fast Red substrate solution for 10 min at room temperature. Sections were then stained with hematoxylin, air-dried, and cover slipped.

Immunofluorescence. Formalin-fixed paraffin embedded (FFPE) tissue sections were deparaffinized using xylene and a series of ethanol washes. After 0.1% Sudan black B (Sigma) treatment to eliminate the autofluorescence background, the sections were heated in Tris-EDTA buffer (10mM Tris Base, 1mM EDTA Solution, 0.05% Tween 20, pH 9.0) for 15 minutes to reverse formaldehyde crosslinks. After rinses with PBS (pH 7.4), the section were blocked with PBT (PBS +0.1% Tween-20) containing 5% normal goat serum overnight at 4°C. Then the sections were incubated with rabbit anti-SARS-CoV Spike (1:200, Sino Biological, 40150-T62-COV2) or mouse anti-SARS-CoV NP (1:200, Sino Biological, 40143-MM05) antibodies and mouse anti-pan-cytokeratin (1:100, Santa Cruz Biotechnology, sc-8018), mouse anti-CC10 (1:100, Santa Cruz Biotechnology, sc-365992), mouse anti-E-cadherin (1:100, Thermo Fisher, 33-4000antibodies for 2 hours at room temperature. After rinses with PBT, the sections were incubated with secondary goat anti-rabbit Alexa Fluor 488 (1:500, Thermo Fisher) and goat anti-mouse Alexa Fluor 568 (1:500, Thermo Fisher) antibodies, for 1 hour at room temperature. Sections were cover slipped using the Vectashield mounting medium with DAPI (Vector Laboratories). Images were captured on a Zeiss LSM 880 confocal system and processed using ImageJ software.

Transmission electron microscopy. Fresh hamster lung and trachea were harvested after euthanasia and submerged in 2.5% glutaraldehyde and 2% paraformaldehyde in 0.1M sodium phosphate buffer for 1-3 hours and then placed in 4% paraformaldehyde for 14 or 21 days for

viral inactivation. Samples were submerged in microchem prior to removal from containment suites. Tissue was trimmed and then rinsed with 0.1M sodium cacodylate buffer before post-fixing with 1% osmium tetroxide in 0.1M sodium cacodylate. After osmium fixation, the samples were rinsed with 0.1M sodium cacodylate buffer, followed by a water wash then subjected to uranyl acetate *en bloc*. Samples were washed with water then dehydrated through a graded ethanol series including 3 exchanges with 100% ethanol. Samples were further dehydrated with equal volume of 100% ethanol and propylene oxide followed by two changes of propylene oxide. Samples were initially infiltrated with equal volumes of propylene oxide and resin (Embed-812; EMS, Hatfield, PA) then incubated overnight in propylene oxide and resin. Next day, the samples were infiltrated with 100% resin embedded and oriented in 100% resin and then allowed to polymerize for 48 hours at 60ºC. 1 micron thick sections were cut from each tissue block, a region of interest for thin sectioning was chosen and 80nm thin sections were cut and collected on 200 mesh copper grids. Two grids from each sample was further contrast stained with 2% uranyl acetate and Reynold's lead citrate. Samples were then imaged on the Jeol 1011 TEM at various magnifications.

Statistical analyses. Statistical analyses were completed using GraphPad Prism 8. Weight data was analyzed using a one-way ANOVA with multiple comparisons for experiments with ≥3 groups; unpaired t-tests were used to analyze weight data for experiments with 2 groups. Comparisons of lymphocyte levels and lung viral load was assessed using unpaired t-tests. Significance of survival data was assessed using log-rank tests. In all analyses, $P<0.05$ is considered statistically significant.

Data availability. All data are available in the main text or the supplementary dataset.

References

1. Cohen J. 2020. From mice to monkeys, animals studied for coronavirus answers. Science 368:221-222.
2. Chan JF, Zhang AJ, Yuan S, Poon VK, Chan CC, Lee AC, Chan WM, Fan Z, Tsoi HW, Wen L, Liang R, Cao J, Chen Y, Tang K, Luo C, Cai JP, Kok KH, Chu H, Chan KH, Sridhar S, Chen Z, Chen H, To KK, Yuen KY. 2020. Simulation of the clinical and pathological manifestations of Coronavirus Disease 2019 (COVID-19) in golden Syrian hamster model: implications for disease pathogenesis and transmissibility. Clin Infect Dis doi:10.1093/cid/ciaa325.
3. Rodgers TF, Zhao, F., Huang, D., Beutler, N., Abbott, R.K., Callaghan, S., Garcia, E., He, W., Hurtado, J., Limbo, O., Parren, M., Peng, L., Ricketts, J., Ricciardi, M.K., Smith, C., Song, G., Woehl, J., Yang, L., Rawlings, S., Smith, D.M., Nemazee, D., Teijaro, J.R., Voss, J.E., Andrabi, R., Briney, B., Landais, E., Sok, D., Jardine, J.G., Burton, D.R. 2020. Rapid isolation of potent SARS-CoV-2 neutralizing antibodies and protection in a small animal model. bioRxiv.
4. Schaecher SR, Stabenow J, Oberle C, Schriewer J, Buller RM, Sagartz JE, Pekosz A. 2008. An immunosuppressed Syrian golden hamster model for SARS-CoV infection. Virology 380:312-21.
5. Huang C, Wang Y, Li X, Ren L, Zhao J, Hu Y, Zhang L, Fan G, Xu J, Gu X, Cheng Z, Yu T, Xia J, Wei Y, Wu W, Xie X, Yin W, Li H, Liu M, Xiao Y, Gao H, Guo L, Xie J, Wang G, Jiang R, Gao Z, Jin Q, Wang J, Cao B. 2020. Clinical features of patients infected with 2019 novel coronavirus in Wuhan, China. Lancet 395:497-506.
6. Kim ES, Chin BS, Kang CK, Kim NJ, Kang YM, Choi JP, Oh DH, Kim JH, Koh B, Kim SE, Yun NR, Lee JH, Kim JY, Kim Y, Bang JH, Song KH, Kim HB, Chung KH, Oh MD, Korea National Committee for Clinical Management of C. 2020. Clinical Course and Outcomes of Patients with Severe Acute Respiratory Syndrome Coronavirus 2 Infection: a Preliminary Report of the First 28 Patients from the Korean Cohort Study on COVID-19. J Korean Med Sci 35:e142.
7. Tan L, Wang Q, Zhang D, Ding J, Huang Q, Tang YQ, Wang Q, Miao H. 2020. Lymphopenia predicts disease severity of COVID-19: a descriptive and predictive study. Signal Transduct Target Ther 5:33.
8. Miao J, Ying B, Li R, Tollefson AE, Spencer JF, Wold WSM, Song SH, Kong IK, Toth K, Wang Y, Wang Z. 2018. Characterization of an N-Terminal Non-Core Domain of RAG1 Gene Disrupted Syrian Hamster Model Generated by CRISPR Cas9. Viruses 10.
9. Goldsmith CS, Tatti KM, Ksiazek TG, Rollin PE, Comer JA, Lee WW, Rota PA, Bankamp B, Bellini WJ, Zaki SR. 2004. Ultrastructural characterization of SARS coronavirus. Emerg Infect Dis 10:320-6.
10. Kim JM, Chung, Y.S., Jo, H.J., Lee, N.J., Kim, M.S., Woo, S.H., Park, S., Kim, J.W., Kim, H.M., Han, M.G. 2020. Identification of Coronavirus Isolated from a Patient in Korea with COVID-19. Osong public health and research perspectives:3-7.
11. Neuman BW, Adair BD, Yoshioka C, Quispe JD, Orca G, Kuhn P, Milligan RA, Yeager M, Buchmeier MJ. 2006. Supramolecular architecture of severe acute respiratory syndrome coronavirus revealed by electron cryomicroscopy. J Virol 80:7918-28.

12. Sahin A, Erdoga, A., Mutla Agaoglu, P., Dineri, Y., Cakirci, A., Senel, M., Okyay, R., Tasdogan, A. 2020. 2019 Novel Coronavirus (COVID-19) Outbreak: A Review of the Current Literature. EMJO:1-7.
13. Ward P, et al. 6 Apr 2020 2020. COVID-19/SARS-CoV-2 Pandemic. https://www.fpm.org.uk/blog/covid-19-sars-cov-2-pandemic/.
14. Vardhana SA, Wolchok JD. 2020. The many faces of the anti-COVID immune response. J Exp Med 217.
15. Boudewijns R, Thibaut, H.J., Katein, S.J.F., Li, R., Vergote, V., Seldeslachts, L., Keyzer, C.D., Sharma, S., Jansen S., Weyenbergh, J.V., Ma, J., Martens, E., Bervoets, L., Buyten, T.V., Jacobs, S., Lui, Y., Marti-Carreras, J., Vanmechelen, B., Wawina-Bokalanga, T., Delang, L., Rocha-Pereira J., Coelmont, L., Chiu, W., Leyssen, P., Heylen, E., Schols, D., Wang, L., CLose, L., Matthijnssens, J., Ranst, M.V., Schramm, G., Laere, K.V., Opdenakker, G., Maes, P., Weynard, B., Cawthorne, C., Velde, G.V., Wang, Z., Neyts, J., Dallmeier, K. 2020. STAT2 signaling as double-edged sword restricting viral dissemination but driving severe pneumonia in SARS-CoV-2 infected hamsters. bioRxiv.
16. Gu J, Gong E, Zhang B, Zheng J, Gao Z, Zhong Y, Zou W, Zhan J, Wang S, Xie Z, Zhuang H, Wu B, Zhong H, Shao H, Fang W, Gao D, Pei F, Li X, He Z, Xu D, Shi X, Anderson VM, Leong AS. 2005. Multiple organ infection and the pathogenesis of SARS. J Exp Med 202:415-24.
17. Min CK, Cheon S, Ha NY, Sohn KM, Kim Y, Aigerim A, Shin HM, Choi JY, Inn KS, Kim JH, Moon JY, Choi MS, Cho NH, Kim YS. 2016. Comparative and kinetic analysis of viral shedding and immunological responses in MERS patients representing a broad spectrum of disease severity. Sci Rep 6:25359.
18. Zhang X, Tan Y, Ling Y, Lu G, Liu F, Yi Z, Jia X, Wu M, Shi B, Xu S, Chen J, Wang W, Chen B, Jiang L, Yu S, Lu J, Wang J, Xu M, Yuan Z, Zhang Q, Zhang X, Zhao G, Wang S, Chen S, Lu H. 2020. Viral and host factors related to the clinical outcome of COVID-19. Nature doi:10.1038/s41586-020-2355-0.
19. Chandrashekar A, Liu J, Martinot AJ, McMahan K, Mercado NB, Peter L, Tostanoski LH, Yu J, Maliga Z, Nekorchuk M, Busman-Sahay K, Terry M, Wrijil LM, Ducat S, Martinez DR, Atyeo C, Fischinger S, Burke JS, Slein MD, Pessaint L, Van Ry A, Greenhouse J, Taylor T, Blade K, Cook A, Finneyfrock B, Brown R, Teow E, Velasco J, Zahn R, Wegmann F, Abbink P, Bondzie EA, Dagotto G, Gebre MS, He X, Jacob-Dolan C, Kordana N, Li Z, Lifton MA, Mahrokhian SH, Maxfield LF, Nityanandam R, Nkolola JP, Schmidt AG, Miller AD, Baric RS, Alter G, Sorger PK, Estes JD, et al. 2020. SARS-CoV-2 infection protects against rechallenge in rhesus macaques. Science doi:10.1126/science.abc4776.
20. Wolfel R, Corman VM, Guggemos W, Seilmaier M, Zange S, Muller MA, Niemeyer D, Jones TC, Vollmar P, Rothe C, Hoelscher M, Bleicker T, Brunink S, Schneider J, Ehmann R, Zwirglmaier K, Drosten C, Wendtner C. 2020. Virological assessment of hospitalized patients with COVID-2019. Nature 581:465-469.
21. Duan K, Liu B, Li C, Zhang H, Yu T, Qu J, Zhou M, Chen L, Meng S, Hu Y, Peng C, Yuan M, Huang J, Wang Z, Yu J, Gao X, Wang D, Yu X, Li L, Zhang J, Wu X, Li B, Xu Y, Chen W, Peng Y, Hu Y, Lin L, Liu X, Huang S, Zhou Z, Zhang L, Wang Y, Zhang Z, Deng K, Xia Z, Gong Q, Zhang W, Zheng X, Liu Y, Yang H, Zhou D, Yu D, Hou J, Shi Z, Chen S, Chen Z, Zhang X, Yang X. 2020. Effectiveness of convalescent plasma therapy in severe COVID-19 patients. Proc Natl Acad Sci U S A 117:9490-9496.

22. Ju B, Zhang Q, Ge J, Wang R, Sun J, Ge X, Yu J, Shan S, Zhou B, Song S, Tang X, Yu J, Lan J, Yuan J, Wang H, Zhao J, Zhang S, Wang Y, Shi X, Liu L, Zhao J, Wang X, Zhang Z, Zhang L. 2020. Human neutralizing antibodies elicited by SARS-CoV-2 infection. Nature doi:10.1038/s41586-020-2380-z.
23. Rogers TF, Zhao F, Huang D, Beutler N, Abbott RK, Callaghan S, Garcia E, He W-t, Hurtado J, Limbo O, Parren M, Peng L, Ricketts J, Ricciardi MK, Smith C, Song G, Woehl J, Yang L, Rawlings S, Smith DM, Nemazee D, Teijaro JR, Voss JE, Andrabi R, Briney B, Landais E, Sok D, Jardine JG, Burton DR. 2020. Rapid isolation of potent SARS-CoV-2 neutralizing antibodies and protection in a small animal model. bioRxiv doi:10.1101/2020.05.11.088674:2020.05.11.088674.
24. Hodge LM, Marinaro M, Jones HP, McGhee JR, Kiyono H, Simecka JW. 2001. Immunoglobulin A (IgA) responses and IgE-associated inflammation along the respiratory tract after mucosal but not systemic immunization. Infect Immun 69:2328-38.
25. Liu J, Babka AM, Kearney BJ, Radoshitzky SR, Kuhn JH, Zeng X. 2020. Molecular detection of SARS-CoV-2 in formalin fixed paraffin embedded specimens. JCI Insight doi:10.1172/jci.insight.139042.

Acknowledgments: We would like to acknowledge the tireless efforts of the Comparative Medicine Division, Histology Lab and Aerobiological Sciences technicians at USAMRIID. We thank Joshua Moore, Jimmy Fiallos, Steven Stephens, Leslie Klosterman, Lynda Miller, Jua Liu, April Babka, Neil Davis and Dave Dyer for assistance with veterinary care, histology and molecular assays, and hematology. Additionally, we thank Brian Kearney, Kathleen Gibson and the Unified Culture Collection for providing the virus.

Funding was provided through the Defense Health Program. The opinions, interpretations, conclusions, and recommendations contained herein are those of the authors and are not necessarily endorsed by the US Department of Defense.

Author contributions were as follows: R.L.B., J.W.G., and J.W.H. designed the study. R.K.K., X.Z., J.A.W., performed the pathology and imaging analyses. L.M.P. and J.M.S. performed the *in vitro* assays. R.L., Y.L., and Z.W. provided the *RAG2* KO animals. D.G., S.Y., and J.G. provided the Centi-F1 mAb. R.L.B. and J.W.H. wrote the paper with all the coauthors.

513 The authors declare no competing interests.

514

515 **Figure Legends**

516 **Fig. 1. CyP-treated, SARS-CoV-2-infected hamsters.** Groups of 10 Syrian hamsters each were
517 immunosuppressed with CyP and **A)** Lymphocyte counts were determined from whole blood 3
518 days (closed symbols) or 4 days (open symbols) following CyP loading dose. CyP administration
519 is depicted by vertical dotted lines in **B)** and **C).** Hamsters were exposed to increasing doses of
520 SARS-CoV-2 intranally on Day 0. **B)** Weights were monitored for 35 days. **C)** Viral RNA copies
521 per pharyngeal swab were assayed at indicated times post-infection. Hamsters were monitored
522 for **D)** survival and **E,F)** lung tissue collected either at the time of death or scheduled euthanasia
523 13 or 35 dpi was assessed for viral load by **E)** RT-PCR and **F)** plaque assay. **G)** Blood was
524 collected from surviving hamsters 35 dpi and assessed by PRNT.

525 **Fig. 2. SARS-CoV-2-infected *RAG2* KO hamsters.** Either *RAG2* KO (n=7) or CyP-treated
526 hamsters (n=10, from Fig. 1) were exposed to 10,000 PFU SARS-CoV-2 on Day 0. Vertical
527 dotted lines in **A)** and **B)** indicate CyP treatment for indicated animals. Hamsters were monitored
528 for **A)** weight and **C)** survival. **B)** Viral RNA copies per pharyngeal swab were assayed at
529 indicated times post-infection. **D)** Organs collected at the time of death were homogenized and
530 assayed for viral load (LU=lung, TR=trachea, HE=heart, LI=liver, SP=spleen, IN=intestine,
531 BR=brain, KI=kidney).

532 **Fig. 3. Pathology of SARS-CoV-2 in CyP-treated and *RAG2* KO hamsters.** H&E sections (**A,**
533 **B**) of lung tissue from CyP-treated hamsters euthanized 13 dpi show extensive areas of
534 consolidation with dense aggregates of inflammatory cells. **A)** Bronchial lumen are lined by
535 hyperplastic folds of respiratory epithelium (asterisk) and the pleural surface is multifocal

thickened and expanded by fibrous connective tissue and inflammatory cells (arrows). **B)** The bronchial lumen are lined by hyperplastic folds of respiratory epithelium (arrow). Areas of alveolar septa lined rows of type 2 pneumocytes (asterisks). **C)** SARS-CoV-2 genomic RNA was frequently detected in alveolar pneumocytes, alveolar infiltrates, and bronchiolar respiratory epithelial cells from CyP-treated hamsters by ISH. H&E sections (**D, E**) of lung tissue from *RAG2* KO hamsters collected at the time of death. **D)** Areas of hemorrhage (asterisk) and inflammation (arrowheads) expanding the interstitium and connective tissue surrounding bronchi and arteries (arrows). **E)** Necrotic bronchial epithelium (arrows) overlaid by hemorrhagic exudate. Peribronchial connective tissue is expanded by lymphocytes, heterophils (asterisks) and fewer macrophages that often contain hemosiderin (arrowheads). There is marked consolidation in surrounding alveoli with marked septal congestion and expansion by previously mentioned inflammatory cells. **F)** SARS-CoV-2 genomic RNA was frequently detected in alveolar pneumocytes, alveolar infiltrates, and bronchiolar epithelial cells from *RAG2* KO hamsters by ISH. (**G-I**) Immunofluorescence assays demonstrate SARS-CoV-2 antigens (S or NP, green) were detected in brochiolar epithelium labelled anti-pan-cytokeratin antibody (red, **G**) club (clara) cells labelled by anti-CC10 antibody (red, **H**) and alveolar epithelial cells labelled by anti-E-cadherin antibody (red, **I**) in *RAG2* KO hamsters. (**J-L**) TEM of hamster lungs with increasing viral loads. **J**) Lung section from hamster with 10^6 molecules of N2 per 100ng RNA. Inset shows cytoplasmic vacuole with possible virus (black arrow). **K**) Lung section from hamster with 10^7 molecules of N2 per 100ng RNA. Potential mature viral particles (approximately 143-154nm diameter, arrowhead) are present at the cell periphery and suspected immature virions are detected more internally in a cytoplasmic vacuole (approximately 62-97nm diameter, black arrow). **L**) Lung section from hamster with 10^8 molecules of N2 per 100ng RNA. Numerous

cytoplasmic vacuoles of possible virus are evident (black arrows). Inset shows an example of swollen rER (asterisk) with virus forming within the swollen rER (black arrow). Scale bars (**A, D**) = 400 microns; (**B**) = 100 microns; (**E**) = 28 microns; (**C, F**) = 100 microns, (**G, H, I**) = 50 microns. (**J-L**) = 1 micron.

Fig. 4. SARS-CoV-2 disrupts the tracheal epithelial layer. Tracheal sections were collected from SARS-CoV-2 infected, CyP-treated hamsters, sorted by lung viral load and analyzed by transmission electron microscopy. **A)** The animal with lung viral load of 10^6 molecules of N2 per 100ng of RNA showed the most intact ciliated cells on the surface of the trachea (arrowheads). As viral load increases (from animals with lung viral load of 10^7 (**B)** and 10^8 (**C)** molecules of N2 per 100ng RNA, respectively) the presence of ciliated cells and epithelial cells lining the trachea lumen decrease. **D)** Cells from the low viral load animal show several cytoplasmic vacuoles with potential immature viral particles (arrows). **E)** The release of cytoplasmic vacuole content (possible immature virions, arrows) into the luminal space of a cell that has detached from the epithelial layer. **F)** From the highest viral load animal, very few ciliated cells are noted. Cytoplasmic vacuole with potential immature viral particles are observed (arrow). Scale bars (**A-C**) = 1 micron; (**D-F**) = 500 nm.

Fig. 5. Re-challenge of previously infected SARS-CoV-2 hamsters. A) Weight data from hamsters initially exposed to 10,000 PFU SARS-CoV-2 and re-challenged with 100,000 PFU SARS-CoV-2. **B)** PRNT80 titers depicting the level of circulating neutralizing antibody prior to Day 43 virus exposure. Disease progression was monitored by **A)** weight and **C)** pharyngeal swabs. Lung tissue collected on Day 50 was assayed for **D)** viral RNA and **E)** infectious virus.

Fig. 6. Passive transfer of anti-SARS-CoV-2 mAb Centi-F1 in immunosuppressed hamsters. Groups of 8 hamsters were immunosuppressed with CyP beginning -3 dpi (and indicated by the vertical lines in **B, C**) and passively transferred 30 mg/kg of Centi-F1 mAb, equivalent volume of normal mAb or PBS -1 dpi and exposed to 1,000 PFU SARS-CoV-2 on Day 0. **A)** Levels of circulating neutralizing antibody from Day 0 serum was assayed by PRNT. Disease progression was monitored by **B)** weight and **C)** pharyngeal swabs. Lung tissue collected 13 dpi was assayed for **D)** viral RNA and **E)** infectious virus.

Fig. 1.

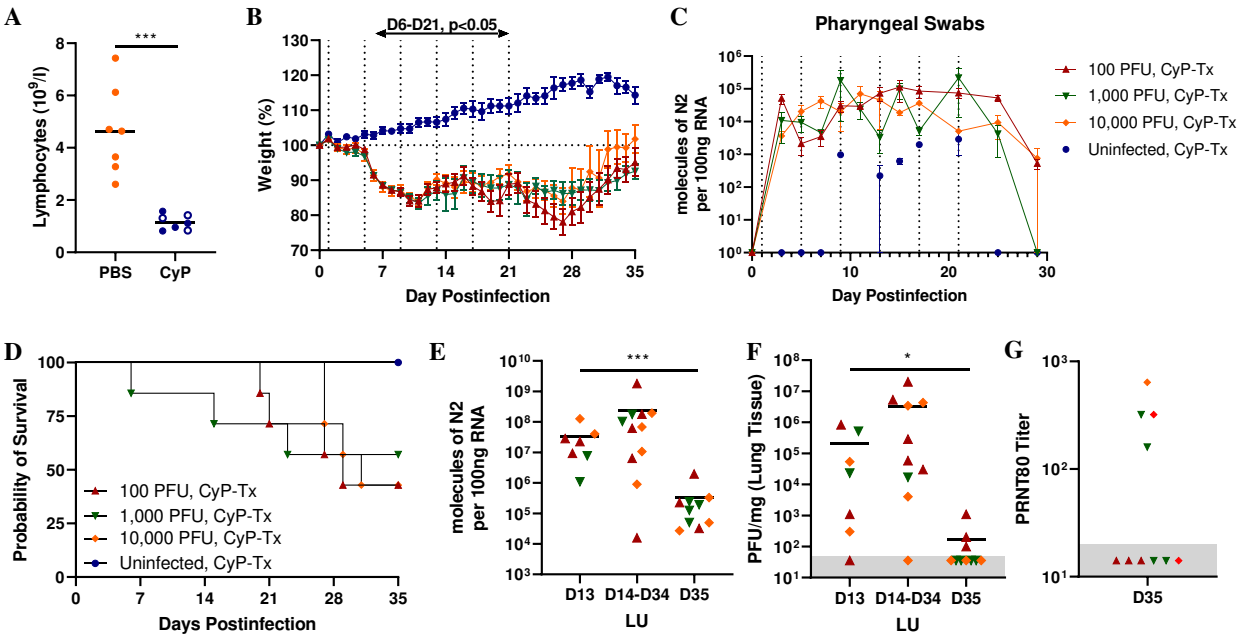

Fig. 2.

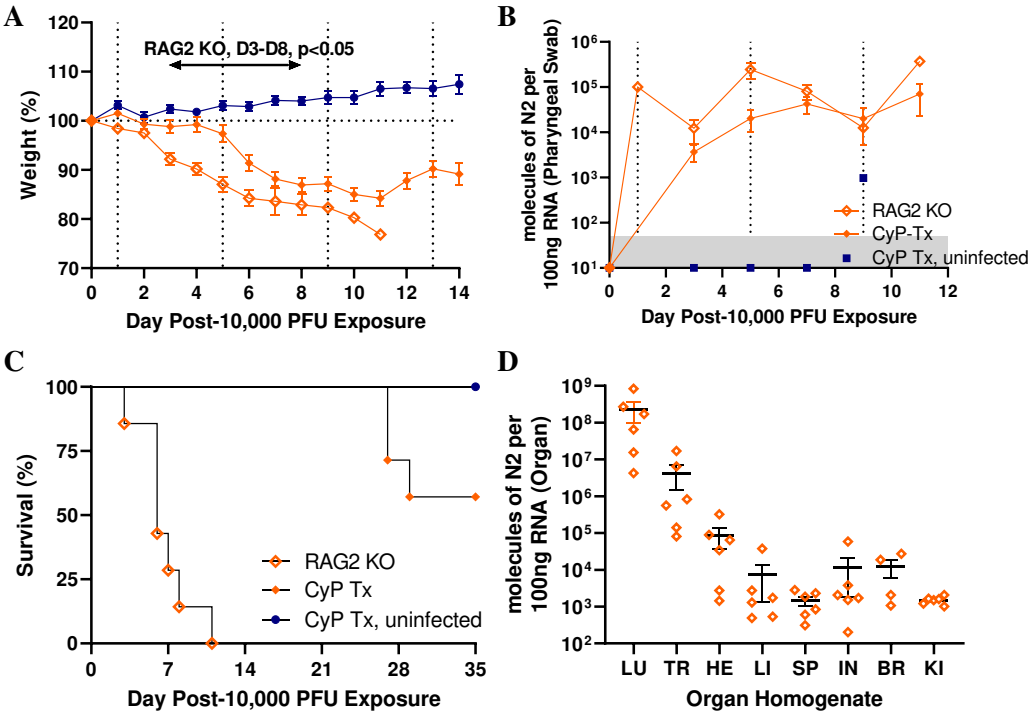

Fig. 3.

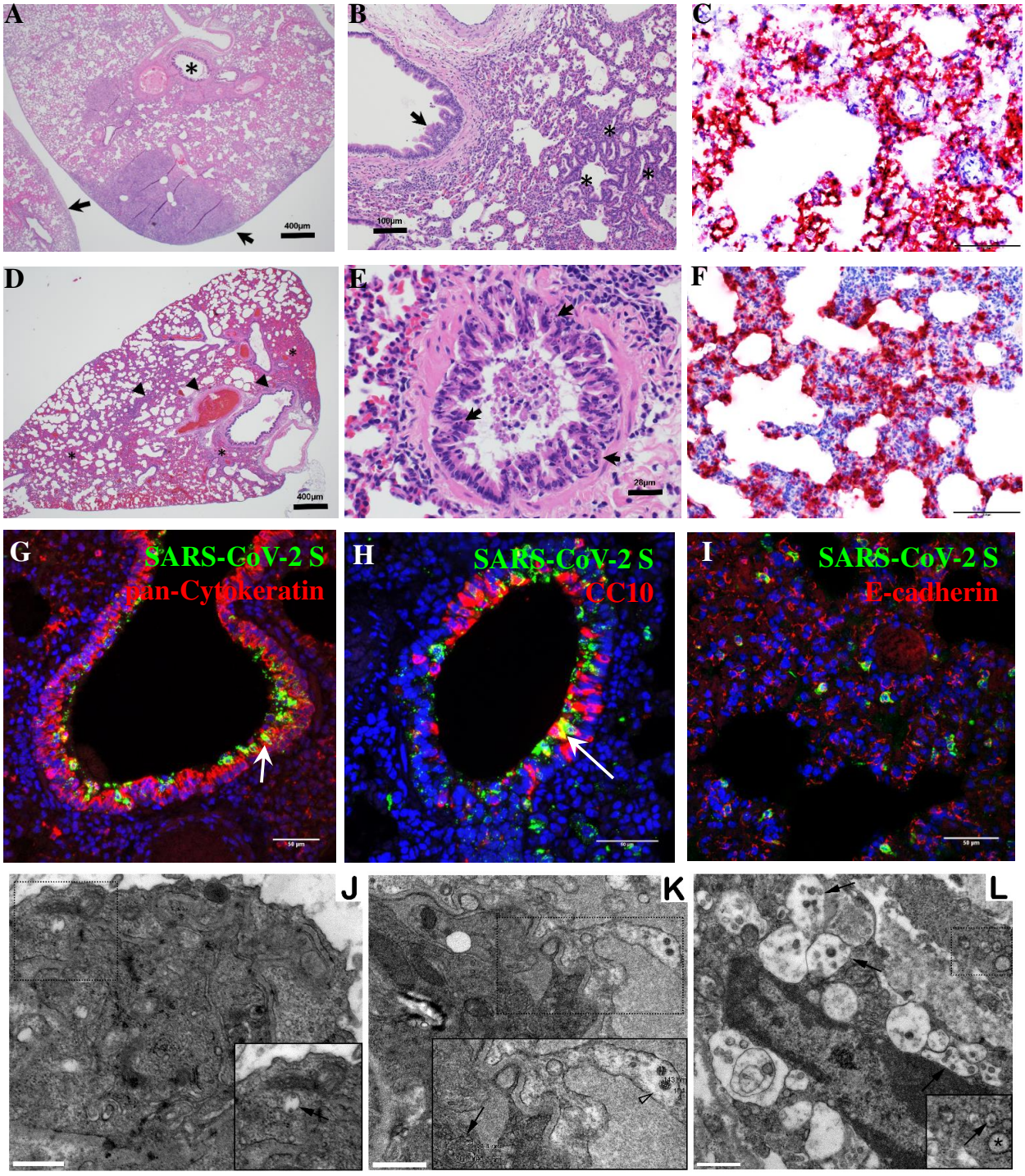

Fig. 4.

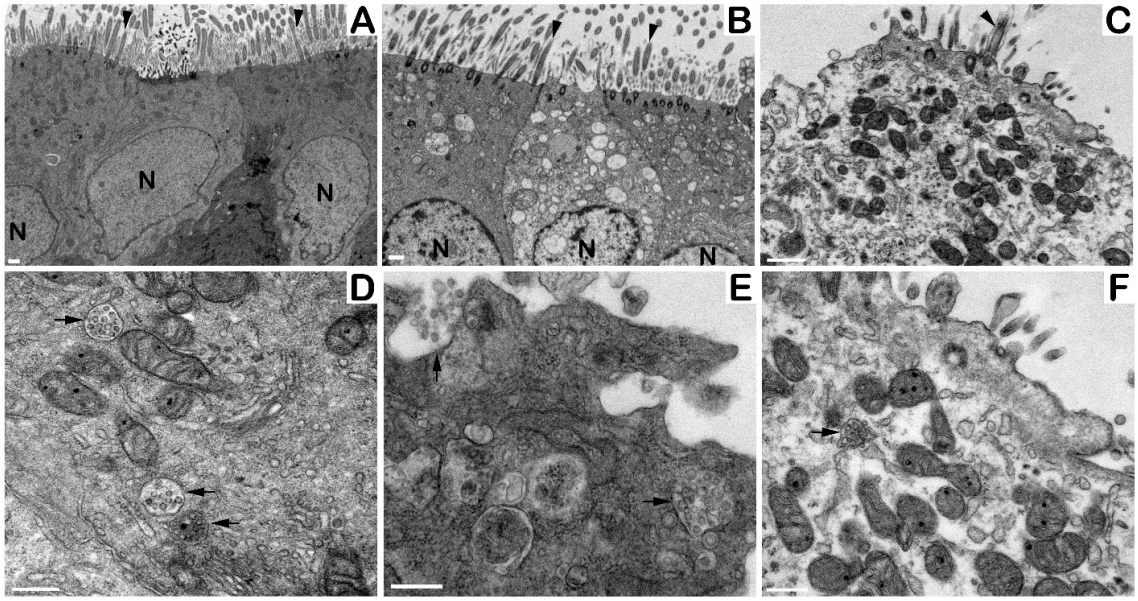

Fig. 5.

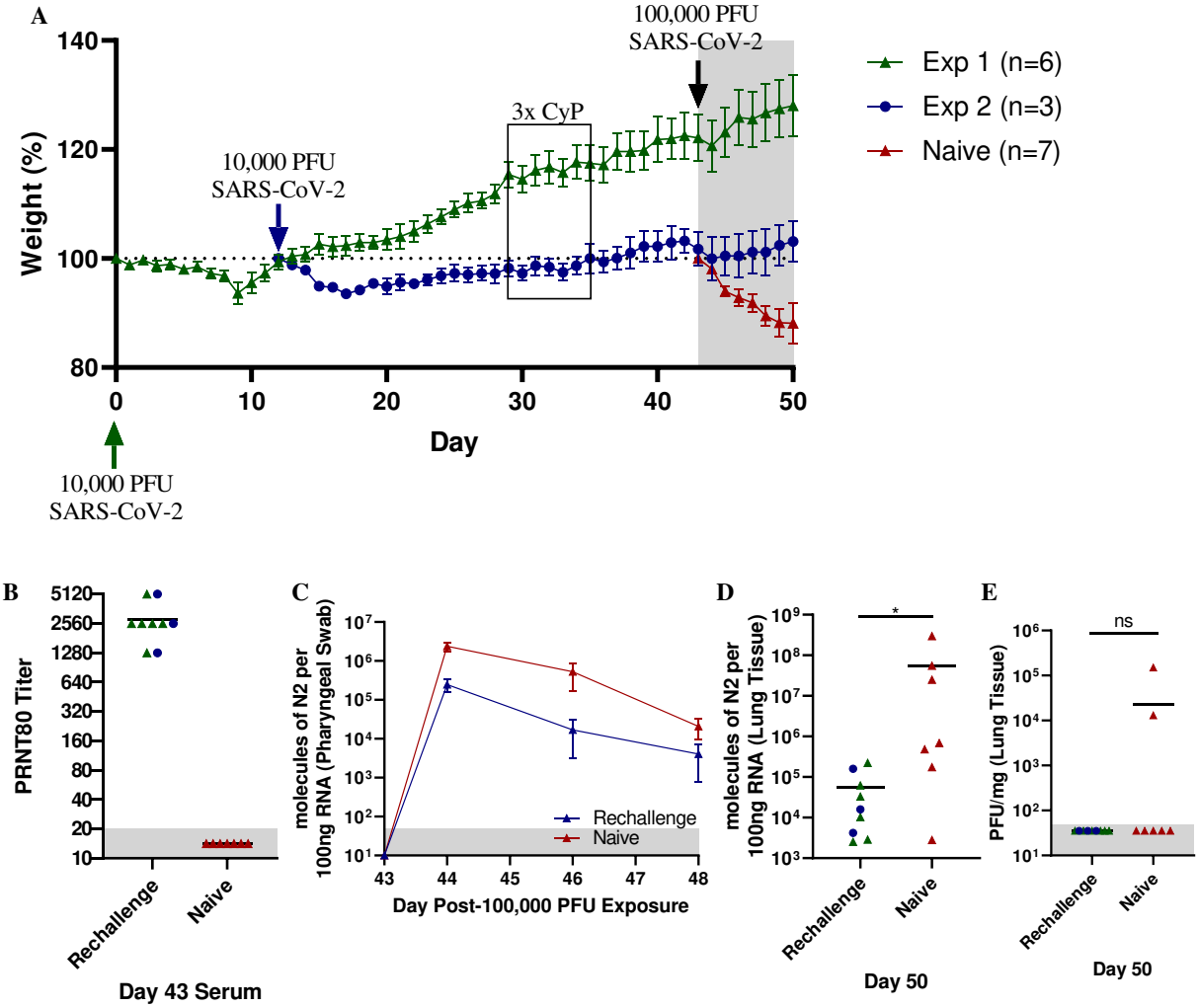

Fig. 6.